

Stress-constrained topology optimization of concrete structures: A preliminary study for combining topology optimization and 3D printing

I. van de Werfhorst-Bouw, H. Hofmeyer, S. Boonstra, R.J.M. Wolfs

Eindhoven University of Technology, the Netherlands

Digital design tools for the 3D Concrete Printing (3DCP) industry could be enriched by topology optimization, among others to minimize the amount of concrete used. However, a prerequisite for applying such an algorithm to 3DCP is that concrete's asymmetric stress limits in tension and compression are correctly addressed. Therefore, here topology optimization is studied as the minimization of the structural volume, subject to local, asymmetric stress constraints, represented by the Drucker-Prager yield criterion. Three available methods have been selected for a comparison: Traditional Topology Optimization (TTO) in combination with the Method of Moving Asymptotes (MMA) by Svanberg (1987); Bi-directional Evolutionary Structural Optimization (BESO); and heuristic Proportional Topology Optimization (PTO). Numerical studies show that TTO provides more optimal results (i.e. a lower structural volume) than BESO and PTO. This is especially clearly shown by some typical benchmarks for which either pure tensile or pure compressive structures are generated. In these benchmarks, it is shown that BESO and PTO generally generate tension-only structures, whereas TTO generally provides more material-efficient compression-only structures. Moreover, TTO shows to be less sensitive to the presence and magnitude of peak stresses in the structure. As such, it is concluded that TTO is preferred over BESO and PTO. Consequently, TTO is applied in an illustrative case study of a two-dimensional façade structure, where a daylight score is presented as an objective or as an additional constraint, and a print path generation tool is applied to the topology optimization outcome. From this case study, although promising, it is concluded that more research is required to obtain a design-for-manufacturing tool that can be utilized in the 3DCP industry.

Key words: Topology optimization, 3D Concrete Printing (3DCP), BESO, PTO, traditional topology optimization, MMA, asymmetric stress constraints

1 Introduction

Topology optimization is a method that is aimed at finding the optimal distribution of material within a given design domain. As such, topology optimization might, for example, be used to obtain higher strength-to-weight ratios of structural elements by avoiding the presence of redundant material. As a result, topology optimization methods are potentially beneficial in the construction industry, e.g. for the design of lighter and less resource intensive structures, which in turn contributes positively to the world-wide problem of resource depletion.

The above potential, across many disciplines, has caused research in the field of topology optimization to see an increasing amount of attention, since the initial publication by Bendsøe and Kikuchi (1988). Based on this first publication, many researchers focused on the maximization of a structure's stiffness, which is equivalent to the minimization of its overall compliance (e.g. Sigmund (2001) or Andreassen, Clausen, Schevenels, Lazarov, and Sigmund (2011)). However, a drawback of these compliance-based methods is that they do not guarantee that stresses in the optimized design are within their limits. And consequently the result is an optimized design that may still require significant post-processing to ensure its structural integrity. Consequently, a slightly newer point of focus is to develop stress-constrained topology optimization, which minimizes the volume, while at the same time satisfying stress constraints. Among others, authors who have worked on stress-constrained volume minimization are Duysinx and Bendsøe (1998), Biyikli and To (2015), and Luo and Kang (2012). Also other objectives, such as the maximization of the first fundamental natural frequency; tuning buckling loads; or the design of compliant mechanisms are all part of the developments (Bruggi & Duysinx, 2012). Reviews in the field of topology optimization can be found in e.g. Bendsøe and Sigmund (2003) and Deaton and Grandhi (2014). Next to a literature review, Deaton and Grandhi (2014) also provide some recommendations related to new algorithm development. The key to these recommendations is that one should focus on methods and test cases that apply to real-world (instead of academic) problems.

A possible real-world application of topology optimization is the development of a design-for-manufacturing tool, in which a digital design can be directly manufactured from its optimized digital model, without the need for post-processing. These kinds of tools may,

for example, be applied in the field of 3D Concrete Printing (3DCP), where ideally a digital model could be sent directly to a concrete printer (Salet, Ahmed, Bos & Laagland, 2018).

Concrete/cement-based additive manufacturing methods have undergone rapid development in recent years, and links with topology optimization have been made successfully. For example, Pastore, Menna and Asprone (2020) investigated topology optimization for combined loading, based on proportional topology optimization with a risk-factor approach to include asymmetric stress limits. Furthermore, a full scale experiment was performed by Kinomura, Murata, Yamamoto, Obi and Hata (2020), who designed a 3D printed, practically scaled pedestrian bridge, for which they used printed segments that were ensembled using pre-stressed bars. However, tensile- and compressive strength asymmetry was neglected in their optimization algorithm. Jewett and Carstensen (2019) designed and constructed three topology optimized beams using either volume-constrained compliance minimization or stress constrained volume minimization (using a so-called p -norm average stress formulation, including asymmetric stress limits in tension and compression) to experimentally validate the optimized geometries. Later, Liu, Jewett and Carstensen (2020) added reinforcement to their analysis by using a hybrid mesh topology optimization algorithm that generates strut-and-tie layouts. However, both above studies only focus on a specific case study and no additive manufacturing method was used to construct the test specimens. Admirable, Langelaar (2018) proposed a method to include manufacturing constraints like a support structure layout and a build orientation into the topology optimization algorithm, for which the volume constrained compliance minimization process was used.

From these previous studies, it can be concluded that direct application of optimization results into a 3DCP manufacturing process requires the consideration of several material- and manufacturing constraints in the optimization algorithm. For example, the material behaviour and asymmetric stress limits of concrete should be correctly incorporated in the optimization process. Therefore, the research presented here focusses on finding the optimization method that has the highest potential to be used in the 3DCP industry. Three topology optimization methods for stress-constrained volume minimization are compared. The main focus of the comparison is on the material behaviour of concrete, which has asymmetric stress limits for tension and compression, and it is investigated whether these properties result in suitable geometries in the optimization. As such, the outcomes of this comparison can provide a start for the development of a design-for-manufacturing tool for

3DCP applications. However, a design-for-manufacturing tool should ideally include more than just stress constraints. Therefore, the most suitable optimization method in this research will be used to investigate the possibilities and limits to adding an extra constraint, a minimum daylight-score, to the optimization process. Furthermore, a print path generation tool for 3DCP is briefly discussed in the context of a façade case study. The paper ends with conclusions and recommendations for future research.

2 State-of-the-art

Structural optimization of concrete structures can be carried out via several means, but here the focus is on topology optimization. For topology optimization, the distribution of material is determined by iterations in which the (relative) densities of discrete parts of the domain are gradually increased or decreased. Besides a design domain and boundary conditions, topology optimization does not require an initial design concept. For initialisation, often a uniform material layout is used. Contrary, size- and shape optimization techniques minimize or maximize a physical (structural) quantity by varying parameters linked to an initial design (Bendsøe & Sigmund, 2003).

In the field of topology optimization, several methods exist. Here, three different methods are studied:

- Traditional Topology Optimization (TTO), which refers to the currently most widely used density-based type of optimization methods. It uses a Solid Isotropic Material with Penalization (SIMP) material model and mathematical gradient-based solvers. Element sensitivities are used to steer the distribution of intermediate densities.
- Bi-directional Evolutionary Structural Optimization (BESO), which is an evolutionary procedure that provides pure black-and-white solutions. Element sensitivities are used to steer the distribution, with elements being either active or not, and so no intermediate densities are used.
- Proportional Topology Optimization (PTO), which is a relatively new method with a fully heuristic and non-gradient based material distribution algorithm. Element compliance or stress values are directly used to steer the (intermediate) distribution, and so no element sensitivities are used.

In literature, several more topology optimization methods can be found, which are either variants of the methods above, or methods that have their origin in shape optimization (such as the level-set method (Challis, 2010)). However, this article focusses only on basic variants of the above-mentioned topology optimization methods, and does not consider the level-set method, since this method has its origin in shape-optimization rather than topology optimization.

2.1 Stress-constrained volume minimization

Stress-constrained volume minimization (in topology optimization) is defined as an optimization problem with the objective to minimize the amount of material within a predefined design domain, while satisfying local or global stress constraints. In the presented study, the design domains of the two-dimensional examples are discretized into square, bilinear, four-node plane stress finite elements with a single integration point at their centre. The stress constraints apply to each individual element. Furthermore, all elements in the design domain have a variable density, with 1.0 representing completely solid material and 0.0 representing a complete void. In mathematical form, the stress-constrained volume minimization problem can then be presented as:

$$\begin{cases} \min.: V(\mathbf{x}) = \sum_{e=1}^N x_e v_e \\ \text{s.t.}: \begin{cases} \sqrt{J_{2D,e}} + \alpha I_{1,e} \leq \beta & \text{for all } e \in \mathbf{N}_e \\ \mathbf{K}(\mathbf{x})\mathbf{u} = \mathbf{f} \\ \mathbf{0} < \mathbf{x}_{\min} \leq \mathbf{x} \leq \mathbf{1} \end{cases} \end{cases} \quad (1)$$

in which $V(\mathbf{x})$ is the total structural volume, v_e is the element volume of element e , and x_e is this element's relative density. Furthermore, $\mathbf{K}(\mathbf{x})$ is the global stiffness matrix, \mathbf{u} and \mathbf{f} are the global displacement and force vectors, N is the number of elements in the discretized design domain, and \mathbf{N}_e describes the set of all elements in the design domain. Finally, $\mathbf{x} = [x_1, x_2, \dots, x_N]^T$ is the vector of design variables, which are all bounded by a minimum value \mathbf{x}_{\min} . Here, the stress constraints are formulated by the Drucker-Prager yield stress criterion, for it can manage asymmetric stress limits in tension and compression, which is a typical material property of concrete (Luo & Kang, 2012). The criterion is denoted as:

$$\sqrt{J_{2D,e}} + \alpha I_{1,e} \leq \beta \quad (2)$$

where α and β are material constants that describe the relation between the material's uniaxial tensile- and compressive strength, $I_{1,e} = \sigma_{xx} + \sigma_{yy} + \sigma_{zz}$ is the first stress invariant of element e , and $J_{2D,e}$ is the second deviatoric stress invariant of element e , expressed by:

$$J_{2D,e} = \frac{1}{6} \left[(\sigma_{xx} - \sigma_{yy})^2 + (\sigma_{yy} - \sigma_{zz})^2 + (\sigma_{zz} - \sigma_{xx})^2 + 6\sigma_{xy}^2 + 6\sigma_{yz}^2 + 6\sigma_{zx}^2 \right] \quad (3)$$

For concrete with a compressive strength σ_{Lc} and a tensile strength σ_{Lt} , the values for α and β can be derived by combining the principal stress states ($\sigma_3 = -\sigma_{Lc}$, $\sigma_1 = \sigma_2 = 0$) and ($\sigma_1 = \sigma_{Lt}$, $\sigma_2 = \sigma_3 = 0$) with the Drucker-Prager yield criterion, which leads to:

$$\alpha = \frac{\sigma_{Lc} - \sigma_{Lt}}{\sqrt{3}(\sigma_{Lc} + \sigma_{Lt})} \quad (4)$$

$$\beta = \frac{2\sigma_{Lc}\sigma_{Lt}}{\sqrt{3}(\sigma_{Lc} + \sigma_{Lt})}. \quad (5)$$

It can be shown that for so-defined strength ratios $\gamma = \sigma_{Lc}/\sigma_{Lt}$ smaller than 1/3 and larger than 3, the Drucker-Prager criterion might give negative results for bi-axial tension or bi-axial compression. To prevent related issues in the topology optimization process, only ratios $1/3 \leq \gamma \leq 3$ are considered here.

3 Topology optimization methods

3.1 Traditional Topology Optimization (TTO)

The first topology optimization method to be presented is Traditional Topology Optimization (TTO). For this method, normally the relationship between an element's Young's modulus (E_e) and the element density follows the SIMP approach, in which the material properties are modelled as the solid material properties multiplied by the element relative density raised to a certain power p (Sigmund, 2001):

$$E_e(x_e) = x_e^p E_0 \quad (6)$$

in which E_0 is the Young's modulus of the solid material, p is the so-called penalty factor, and x_e is the relative density of element e , which should always be larger than a small, non-zero value x_{\min} to prevent singularity of the stiffness matrix (Sigmund, 2001). The power-law approach steers the topology optimization procedure as much as possible towards black-and-white designs, e.g. designs with most if not all densities close to either 0.0 or 1.0.

Using the material model above, several strategies can be used to predict the material (re)distribution per iteration. For the stress-constrained problem here – which has multiple constraints – the Method of Moving Asymptotes (MMA) is applied, using an implementation by Svanberg (1987). In the MMA method, each iteration starts with a current iteration state \mathbf{x}^k , in which \mathbf{x} is the vector of design variables and k is the iteration number. At this state \mathbf{x}^k , each constraint function $f_i(\mathbf{x})$ is replaced by a convex approximation function, based on gradient information and on its two parameters u_i^k and l_i^k , which are defined as the *moving asymptotes*. Then the sub problem with the convex functions is solved, resulting in a new iteration point \mathbf{x}^{k+1} , including updated values for the moving asymptotes (Svanberg, 1987). Note that sensitivity information of both the objective and the constraint functions is required. For a detailed description of MMA, the calculation of approximating functions, and the so-called primal-dual Newton method that is used to solve the sub problems, the reader is referred to Svanberg (1987) and Svanberg (2002).

Each constraint function in this research is formulated via the Drucker-Prager yield function (Equation 2), which is here a function of the stress state at the integration point at the centre of each element. Following normal finite element theory, the (homogenized macroscopic) stress state $\boldsymbol{\sigma}_{e,\text{hom}}$ at the centre of an element with relative density x_e is related to the element displacement vector \mathbf{u}_e by $\boldsymbol{\sigma}_{e,\text{hom}} = x_e^p \mathbf{T}_0 \mathbf{u}_e$, in which $\mathbf{T}_0 = E_0 \mathbf{D}_0 \mathbf{B}_e$ is the stress matrix of the element with solid material (density 1.0), which can be derived using the finite element's shape function derivative matrix \mathbf{B}_e and its constitutive matrix \mathbf{D}_0 (the latter omitting Young's modulus $E_e(x_e)$). However, this (homogenized macroscopic) stress differs from the stresses in a fictitious porous microstructure of an element with an intermediate density (the latter to be regarded as consisting of finely distributed solid parts with voids in between). Therefore, Duysinx and Bendsøe (1998) state that the failure criteria for a porous (i.e. intermediate density) SIMP material should be based on the so-called *local* element stress state $\boldsymbol{\sigma}_e$, being the stress in the solid parts of the porous microstructure. They predict this *local* stress state by interpolation as follows:

$$\boldsymbol{\sigma}_e = \frac{\boldsymbol{\sigma}_{e,\text{hom}}}{x_e^q} = x_e^{p-q} \mathbf{T}_0 \mathbf{u}_e \quad (7)$$

for which the power q should be taken equal to p to obtain a response that corresponds to the behavior of porous materials. This means that the density-related term x_e in Equation 7

vanishes. Note that the stress is still an implicit function of the relative density though, for the relative density distribution has determined the displacements \mathbf{u}_e in the finite element analysis earlier.

A combination of Drucker-Prager based stress constraints and the above stress formulation for a porous microstructure, $\sigma_e = \mathbf{T}_0 \mathbf{u}_e$, may give rise to the so-called *singularity phenomenon*, in which the algorithm cannot lower the density of low-density elements to void level (x_{\min}). To prevent the *singularity phenomenon*, the constraint function is modified by the ε -relaxation technique (Duysinx & Sigmund, 1998). Thus, relaxing the Drucker-Prager yield stress criterion and using matrix notation for Equation 2, leads to the final expression for a constraint function for each element e :

$$R_e = \frac{1}{\beta} \left(\left(\frac{1}{3} \mathbf{u}_e^T \mathbf{M}_0 \mathbf{u}_e \right)^{\frac{1}{2}} + \alpha \mathbf{W}_0 \mathbf{u}_e \right) - h_e \leq 0 \quad e \in \mathbf{N}_e \quad (8)$$

with $\mathbf{M}_0 = \mathbf{T}_0^T \mathbf{V} \mathbf{T}_0$ and $\mathbf{W}_0 = \mathbf{w}^T \mathbf{T}_0$, in which \mathbf{w} and \mathbf{V} are a constant vector and matrix, which are introduced for computing the first and second stress invariants as mentioned in section 2. Furthermore, $h_e = 1 - \varepsilon + \varepsilon/x_e$ is the relaxation coefficient. The relaxation parameter ε is a small number, which is taken as $\varepsilon = \sqrt{x_{\min}}$ in this research, based on the publication of Luo and Kang (2012). The sensitivity of each stress constraint R_e ($e \in \mathbf{N}_e$) with respect to the element densities x_j ($j \in \mathbf{N}_e$) is obtained via direct differentiation of Equation 8:

$$\frac{\partial R_e}{\partial x_j} = \frac{1}{\beta} \left(\frac{1}{3} \left(\frac{1}{3} \mathbf{u}_e^T \mathbf{M}_0 \mathbf{u}_e \right)^{-\frac{1}{2}} \mathbf{u}_e^T \mathbf{M}_0 \frac{\partial \mathbf{u}_e}{\partial x_j} + \alpha \mathbf{W}_0 \frac{\partial \mathbf{u}_e}{\partial x_j} \right) + \delta_{ej} \frac{\varepsilon}{x_e^2} \quad (9)$$

in which δ_{ej} ensures that the last term is zero, except for $e = j$. Equation 9 can be simplified by defining a sparse vector \mathbf{a}_e that has the same dimensions as the global displacement vector \mathbf{u} and that contains non-zero elements only at the positions corresponding to the (global) degrees of freedom of element e in \mathbf{u} , here symbolically presented as:

$$\mathbf{a}_e = \left[0 \dots 0 \left(\frac{\mathbf{u}_e^T \mathbf{M}_0}{\sqrt{3 \mathbf{u}_e^T \mathbf{M}_0 \mathbf{u}_e}} + \alpha \mathbf{W}_0 \right) 0 \dots 0 \right]^T \quad (10)$$

Which transforms Equation 9 into:

$$\frac{\partial R_e}{\partial x_j} = \frac{1}{\beta} \mathbf{a}_e^T \frac{\partial \mathbf{u}}{\partial x_j} + \delta_{ej} \frac{\varepsilon}{x_e^2}. \quad (11)$$

By taking the derivative of the equilibrium equation $\mathbf{K}(\mathbf{x})\mathbf{u} = \mathbf{f}$ on both sides, and neglecting body forces (e.g. self-weight), such that $\partial \mathbf{f} / \partial x_j = 0$, it is obtained that:

$$\frac{\partial R_e}{\partial x_j} = -\frac{1}{\beta} \mathbf{a}_e^T \mathbf{K}^{-1} \mathbf{L}_j^T p x_j^{p-1} E_0 \mathbf{K}_{0,j} \mathbf{u}_j + \delta_{ej} \frac{\varepsilon}{x_e^2} = -\frac{1}{\beta} (\mathbf{L}_j \boldsymbol{\lambda}_e)^T p x_j^{p-1} E_0 \mathbf{K}_{0,j} \mathbf{u}_j + \delta_{ej} \frac{\varepsilon}{x_e^2} \quad (12)$$

where $\mathbf{K}_{0,j}$ is the element stiffness matrix without Young's modulus, and the matrix \mathbf{L}_j collects nodal displacements from the global displacement vector via $\mathbf{L}_j \mathbf{u} = \mathbf{u}_j$. Furthermore, vector $\boldsymbol{\lambda}_e$ is the solution to the adjoint system of equations $\mathbf{K} \boldsymbol{\lambda}_e = \mathbf{a}_e$.

The sensitivities of the stress constraints in Equation 12 form a Jacobian matrix, representing the partial derivatives of each stress constraint to each design variable. The sensitivity of the objective function with respect to one of the design variables ($\partial V / \partial x_e$) equals the element volume divided by the total volume (v_e / V_0), which is constant for the regular mesh used here. To prevent the formation of checkerboard patterns and mesh-dependent results, a density filter is applied (Sigmund, 2007). This filter results in filtered *physical densities* (\tilde{x}_e) next to the *design variables* (x_e). The design variables are filtered by taking a weighted average over the densities in a circular filter area with radius r_{\min} :

$$\tilde{x}_e = \frac{\sum_{i \in \mathbf{N}_e} H_{ei} x_i}{\sum_{i \in \mathbf{N}_e} H_{ei}} \quad (13)$$

with the height factor $H_{ei} = \max(0, r_{\min} - \Delta(e, i))$, in which r_{\min} is the filter radius, $\Delta(e, i)$ is the distance between the center of elements e and i , and H_{ei} is zero outside the filter area. The *physical densities* are the ones used in the finite element analysis. And after this analysis, the sensitivities of the objective- and constraint functions with respect to the *design variables* are found by:

$$\frac{\partial V}{\partial x_j} = \sum_{i \in \mathbf{N}_e} \frac{\partial \tilde{x}_i}{\partial x_j} \frac{\partial V}{\partial \tilde{x}_i} = \sum_{i \in \mathbf{N}_e} \frac{H_{ji} \frac{\partial V}{\partial \tilde{x}_i}}{\sum_{m \in \mathbf{N}_e} H_{im}} = \sum_{i \in \mathbf{N}_e} \frac{H_{ji} \frac{v_i}{V_0}}{\sum_{m \in \mathbf{N}_e} H_{im}} \quad (14)$$

$$\frac{\partial R_e}{\partial x_j} = \sum_{i \in \mathbf{N}_e} \frac{\partial \tilde{x}_i}{\partial x_j} \frac{\partial R_e}{\partial \tilde{x}_i} = \sum_{i \in \mathbf{N}_e} \frac{H_{ji} \frac{\partial R_e}{\partial \tilde{x}_i}}{\sum_{m \in \mathbf{N}_e} H_{im}} \quad (15)$$

which are obtained by the chain rule, and which describe the sensitivity to the *design variables* instead of the sensitivity to the *physical densities*. As such, the density filter ensures that a consistent optimization problem is maintained, in which the *physical densities* are used for the finite element analyses and the *design variables* for the optimization process. Using the above setup, the solution procedure for stress-constrained TTO is schematically shown in Figure 1. Note that for comparison with the other methods to be presented, TTO updates element densities based on objective and constraint *sensitivities* (to the element densities), and intermediate densities are possible.

TTO - stress-constrained volume minimization (with density filter)		
1. Set initial (physical) densities:		$\tilde{\mathbf{x}} = \mathbf{x}$
2. Finite element analysis:		$\mathbf{K}(\tilde{\mathbf{x}})\mathbf{u} = \mathbf{f}$
3. Objective- and constraint functions:		$\min V(\tilde{\mathbf{x}}) = \sum \tilde{x}_e v_e$ $\sqrt{J_{2D}(\tilde{\mathbf{x}})} + \alpha I_1(\tilde{\mathbf{x}}) - \beta h_e \leq 0$
4. Sensitivity analysis:		$\frac{\partial R_e}{\partial \tilde{x}_j}, \frac{\partial V}{\partial \tilde{x}_j}$
5. Sensitivities as function of design variables:		$\frac{\partial R_e}{\partial \tilde{x}_j} \rightarrow \frac{\partial R_e}{\partial x_j}, \frac{\partial V}{\partial \tilde{x}_j} \rightarrow \frac{\partial V}{\partial x_j}$
6. Update design variables by MMA:		$\mathbf{x}_{\text{new}} \left(R_e, \frac{\partial R_e}{\partial x_j}, V, \frac{\partial V}{\partial x_j} \right)$
7. Find new physical densities via filtering:		$\mathbf{x}_{\text{new}} \rightarrow \tilde{\mathbf{x}}_{\text{new}}$
8. Check convergence:	Stable solution?	yes: finished // no: go to 2

Figure 1. Schematic overview of Traditional Topology Optimization (TTO) for stress-constrained volume minimization

3.2 Bi-directional Evolutionary Structural Optimization (BESO)

In the group of Evolutionary Structural Optimization (ESO) methods, densities do not have any value between 0.0 and 1.0, as in the SIMP approach. Instead, they are either 1.0 or 0.0 (black or white, solid or void). Consequently, the expression for the Young's modulus becomes:

$$E_e(x_e) = \max(E_{\min}, x_e E_0) \quad x_e = 0.0 \vee x_e = 1.0 \quad (16)$$

in which E_{\min} is a small, non-zero stiffness assigned to void regions, to prevent singularity of the stiffness matrix.

The ESO method was developed based on the idea that a structure will obtain its optimal topology by gradually removing low-stressed material from an initially fully occupied design domain (Xie & Steven, 1997). However, it was shown that this approach does not always work if removed elements cannot be recovered (Xia, Xia, Huang, & Xie, 2018). Consequently, the Bi-directional ESO (BESO) method was developed, which also allows for the recovery of void elements in the neighbourhood of highly-stressed full density elements. Several variants of the BESO method exist. The BESO method that is applied here uses sensitivity information to determine whether to add or remove an element. And by using a sensitivity filter, the sensitivities with respect to the design variables for both solid and void elements are computed consistently (Deaton & Grandhi, 2014).

A stress-constrained volume minimization problem can be solved by BESO by starting with a fully occupied design domain and determining a new target volume per iteration. This target volume can either be higher or lower than the volume of the previous iteration, based on whether the stress constraints are violated or not:

$$V^k = \begin{cases} V^{k-1}(1+c_{er}) & \text{if } R_{e,\max} > 0 \\ V^{k-1}(1-c_{er}) & \text{if } R_{e,\max} < 0 \end{cases} \quad (17)$$

in which V^k is the target volume at iteration k , c_{er} is a predefined evolutionary ratio, which determines the percentage of material to be removed or added in each iteration, and $R_{e,\max}$ is the maximum value of all stress constraints. The target volume of the current iteration is distributed over the design domain based on the following threshold parameter α^{th} for material addition and deletion:

$$x_e^{k+1} = \begin{cases} 0 & \text{if } |\hat{a}_e^k| \leq \alpha^{th} \text{ and } x_e^k = 1 \\ 1 & \text{if } |\hat{a}_e^k| > \alpha^{th} \text{ and } x_e^k = 0 \\ x_e^k & \text{otherwise} \end{cases} \quad (18)$$

in which \hat{a}_e represents the filtered and averaged (to be explained) sensitivity of element e . Note that the threshold parameter α^{th} is set in each step by means of a bisection method, such that the target volume in Equation 17 will be obtained (see also the pseudocode in Figure 2). The sensitivity numbers α_j ($j \in \mathbf{N}_e$) are based on the magnitude of the sensitivity of the stress constraints with respect to the design variables. The computation of these sensitivities is similar to the sensitivity analysis presented for the TTO method, with the

exception that no intermediate densities exist in BESO. Therefore, stress interpolation and constraint relaxation are not required, which leads to:

$$R_e = \frac{x_e}{\beta} \left(\left(\frac{1}{3} \mathbf{u}_e^T \mathbf{M}_0 \mathbf{u}_e \right)^{\frac{1}{2}} + \alpha \mathbf{W}_0 \mathbf{u}_e \right) - 1 \leq 0 \quad e \in \mathbf{N}_e \quad (19)$$

in which the element relative density x_e equals either 0 or 1. If $x_e = 0$ (void), Equation 19 becomes $R_e = -1$, so the stress-constraints for void elements are satisfied naturally.

Consequently, only solid elements are considered in the sensitivity analysis. For these solid elements ($x_e = 1$), the sensitivity of Equation 19 with respect to the design variables is determined similar to the sensitivity analysis presented in Section 3.1. However, the result of that sensitivity analysis will be a full Jacobian matrix, while the sensitivity data in BESO should exist of only one value per element to allow for ordering of the sensitivities. As such, reducing the Jacobian matrix is achieved by selecting for each element only the sensitivity that belongs to that constraint that shows the maximal sensitivity for the element's relative density, as follows:

$$\alpha_j = \max_{e \in \mathbf{N}_e} \left(\left| \frac{\partial R_e}{\partial x_j} \right| \right) = \max_{e \in \mathbf{N}_e} \left(\left| -\frac{1}{\beta} (\mathbf{L}_j \boldsymbol{\lambda}_e)^T E_0 \mathbf{K}_{0,j} \mathbf{u}_j \right| \right) \quad (20)$$

Note that $\partial R_e / \partial x_j$ equals 0 if R_e concerns a void element, to be consistent with Equation 19 for solid ($x_e = 1$) or void ($x_e = 0$) elements. This correction also follows the research performed by Xia, Zhang, Xia and Shi (2018). For reasons mentioned previously for TTO, the sensitivity numbers α_j in Equation 20 are filtered using a sensitivity filter:

$$\tilde{\alpha}_e = \frac{\sum_{j \in \mathbf{N}_e} H_{ej} \alpha_j}{\sum_{j \in \mathbf{N}_e} H_{ej}} \quad (21)$$

After which they are averaged with the sensitivities of the *previous* iteration:

$$\hat{\alpha}_e^k = \frac{\tilde{\alpha}_e^k + \tilde{\alpha}_e^{k-1}}{2} \quad (22)$$

This latter inclusion of history information has shown to improve convergence and to prevent strong oscillations. An overview of the BESO procedure above is schematically presented in Figure 2. For comparison with the other methods, note that BESO updates element densities based on *sensitivities* of the constraints to the element densities, but

elements are either present (full density) or do not exist (zero density), so no intermediate densities are used.

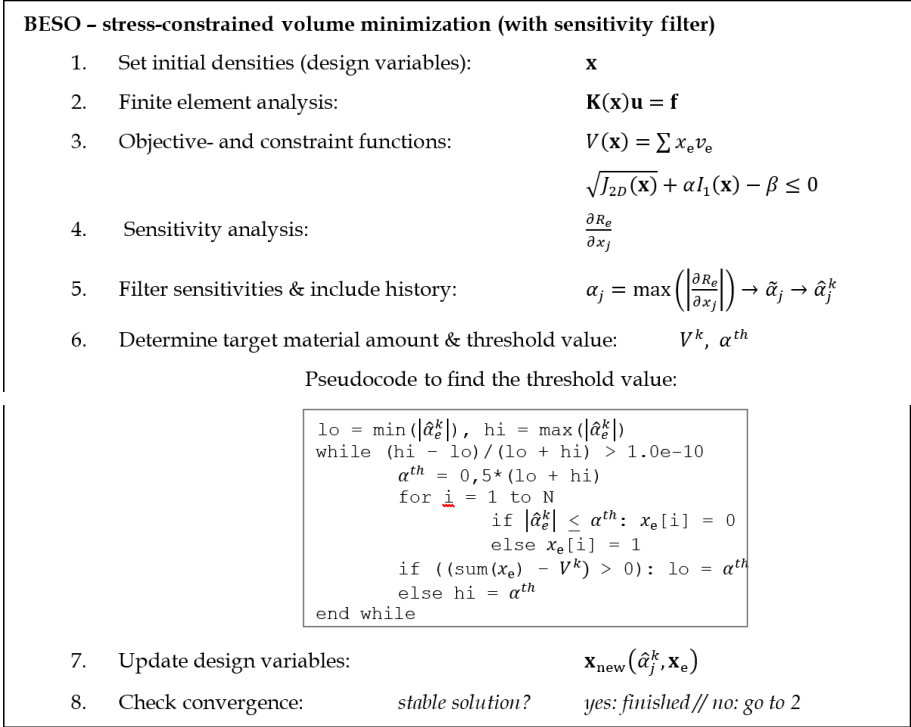


Figure 2. Schematic overview of Bi-directional Evolutionary Structural Optimization (BESO) for stress-constrained volume minimization

3.3 Proportional Topology Optimization (PTO)

As for TTO, the material properties in the PTO method are described by the SIMP material model, Equation 6. However, different from TTO, updating of the design variables does not utilize sensitivities (of the stress constraints to the densities). Instead, densities are distributed proportional to the element stress itself. Additionally, Biyikli and To (2015) suggest that PTO performs better if the above proportional relationship is extended with a power q , with $q = 2$ being the optimum value. This leads to:

$$x_{e,new} = \frac{m_r \sigma_{eq,e}^q}{\sum_{i \in N_e} \sigma_{eq,i}^q} \quad (23)$$

with $\sigma_{eq,e}$ an equivalent stress in the element, to be presented below, and m_t the so-called remaining material amount, which is determined iteratively by an inner loop of the solution procedure, and that depends on the target material amount per iteration m_t . This target material amount per iteration (m_t) is based on whether the stresses in the structure exceed their limits or not:

$$m_t = \begin{cases} (\sum_{e=1}^N x_e + 0.001N)v_e & \text{if } \sigma_{eq,max} > \sigma_{lim} \\ (\sum_{e=1}^N x_e - 0.001N)v_e & \text{if } \sigma_{eq,max} < \sigma_{lim} \end{cases} \quad (24)$$

in which N is the number of elements in the design domain and σ_{lim} is the stress limit for the maximum equivalent Drucker-Prager yield value ($\sigma_{eq,max}$). The parameter $\sigma_{eq,e}$ in Equation 23 is derived from the Drucker-Prager yield criterion, Equation 2, which is rewritten to the form:

$$\sigma_{eq,e} = \frac{\sigma_{Lt}}{\beta} \left(\sqrt{J_{2D,e}} + \alpha I_{1,e} \right) \leq \sigma_{Lt} \quad (25)$$

which states that the tensile strength (σ_{Lt}) is the limit for the equivalent Drucker-Prager stress value at the center of the element ($\sigma_{eq,e}$). Note that Equation 25 could also have been formulated in terms of the compressive rather than the tensile strength, because α and β are functions of both the tensile and compressive strength. To determine the values of the stress invariants ($J_{2D,e}$ and $I_{1,e}$), the homogenized macroscopic stress at the center of the element is used ($\sigma_{e,hom} = x_e^p \mathbf{T}_0 \mathbf{u}_e$). This means that grey elements are interpreted as solid elements with a lowered Young's modulus. Note that in TTO grey elements are interpreted as microstructures that exist of partly solid material and partly voids. For solid ($x_e = 1.0$) and void ($x_e = 0.0$) elements, as shown to be often found in the solutions, there is no difference in interpretation, and therefore the general conclusions of this research still hold. Besides, researched showed that by using the formulation of *local* stresses in PTO (as in TTO) the PTO algorithm is not able to find any suitable results due to the *singularity phenomenon* (Duysinx & Sigmund, 1998), i.e. the algorithm is incapable of lowering the density of low-density elements to void level.

The densities that are found from the proportional distribution ($x_{e,new}$), Equation 23, are filtered using a density filter:

$$\tilde{x}_e = \frac{\sum_{i \in N} H_{ei} x_{i,new}}{\sum_{i \in N} H_{ei}} \quad (26)$$

Due to the proportional distribution of the design variables, the densities can be assigned values larger than 1 or smaller than 0. To prevent this, the values of the filtered densities (\tilde{x}_e) are cut-off at their limits, making the actual material amount (m_a) different from the target material amount (m_t). To resolve this issue, the remaining material amount must be determined and redistributed multiple times in an inner loop of the solution procedure, until m_a is sufficiently close to m_t . The above PTO method is schematically presented in Figure 3. For comparison with the other methods: PTO updates element densities based on element (equivalent) stress *values*, not sensitivities, and intermediate densities are used.

4 Numerical results and comparison

This section presents a comparison of the three topology optimization methods in Section 3, for future application in the field of 3DCP, and with therefore a focus on the asymmetric stress limits that are typical for concrete.

4.1 Convergence

The iterative predictions (density updates) in each optimization algorithm can be halted at the moment that a final design state is reached. For now, it is assumed that a final state is obtained if the objective value is stable (i.e. constant) over 10 iterations. This is described

PTO - stress-constrained volume minimization (with density filter)		
1. Set initial (physical) densities:	$\tilde{\mathbf{x}} = \mathbf{x}$	
2. Finite element analysis:	$\mathbf{K}(\tilde{\mathbf{x}})\mathbf{u} = \mathbf{f}$	
3. Objective- and constraint functions:	$V(\tilde{\mathbf{x}}) = \sum \tilde{x}_e v_e$	
	$\sqrt{J_{2D}(\tilde{\mathbf{x}})} + \alpha I_1(\tilde{\mathbf{x}}) - \beta \leq 0$	
4. Determine target- and remaining material amount:	m_t, m_r	
a. Find new densities (proportional distribution):	$x_{e,new} = \frac{m_r \sigma_{eq,e}^q}{\sum_{i \in N} \sigma_{eq,i}^q}$	
b. Apply density filter & cut-off at limits:	$\tilde{\mathbf{x}}_{new}$	
c. Calculate actual material amount:	$m_a = \sum x_{e,new} v_e$	
d. Update m_r and check convergence:	$m_r = m_t - m_a$	
	$m_r < threshold?$	yes: go to 5 // no: go to 4a
5. Check convergence:	stable solution?	yes: finished // no: go to 2

Figure 3. Schematic overview of Proportional Topology Optimization (PTO) for stress-constrained volume minimization

by the equation below, for which its evaluation is started after the number of iterations k is larger than $2M$:

$$\frac{\left| \sum_{i=1}^M (\delta^{k-i+1} - \delta^{k-M-i+1}) \right|}{\sum_{i=1}^M \delta^{k-i+1}} < \delta_{err} \quad (27)$$

in which g is the objective, δ_{err} is a threshold value, and M determines the number of iterations that should be stable (for $M = 5$, the objective should be stable over 10 iterations). Regardless, a minimum of 50 iterations is always carried out, to prevent premature abortion at a non-optimal configuration. Finally, for the BESO and PTO simulations, a convergence graph is studied afterwards to check if the most optimal solution is found, or if a more optimal solution can be obtained by stopping the iterations earlier, see also Section 4.7.

4.2 Benchmark tests

Concrete has asymmetric stress limits for tension and compression. Therefore, the results of the optimization algorithms are, among others, compared by benchmark tests that are known for their typical results in case of asymmetric stress limits.

To illustrate this, the first benchmark test is a single rod structure with an axial load acting at mid-span, Figure 4. The amount of material in the rod might be minimized by transforming the structure into either a tensile or compressive rod with a length of half of the original single rod structure. If the stress limit of the material in compression is higher than the stress limit in tension (e.g. $\sigma_{Lc} = 2\sigma_{Lt}$), the required cross-sectional area of the tensile rod ($A_t = F/\sigma_{Lt}$) will be larger than the required cross-sectional area of the compressive rod ($A_c = F/\sigma_{Lc} = F/(2\sigma_{Lt})$). For at least simple geometries, likely this statement may be generalized as follows: if a concrete structure (with a higher compressive than tensile strength) has the possibility to form only members with either compressive or tensile stresses, during a volume minimization subject to stress constraints, it should form the configuration with only compressive members to obtain the lowest structural volume.



Figure 4. Minimizing the volume of a single rod (complete left) by transforming it into a tensile (middle) or compressive rod (complete right)

Several characteristically similar benchmark problems are carried out and discussed in the upcoming sections. Note that these are still academic cases for which fictive material properties are used.

4.3 Single rod benchmark

This first benchmark study simulates the above single rod element with an axial load acting at mid-span. This single rod is modelled as a 2D optimization problem, using two four-node plane stress finite elements and two horizontal concentrated loads. The design domain, boundary conditions and loads are presented in Figure 5. The two concentrated loads (F) have a magnitude of 0.5 N each. The plane stress elements are 1×1 mm, and have a thickness (t) of 1 mm too. The Young's modulus (E) of the solid material is 1 MPa, the Poisson's ratio (ν) is 0.3, and the tensile and compressive strengths are 1 and 1.25 MPa, respectively. The penalty factor (p) is 3 and filtering is ignored ($r_{\min} = 1$). The first step of the stress-constrained volume minimization is explained for each of the three optimization methods, and results of the optimizations are given in Table 1.

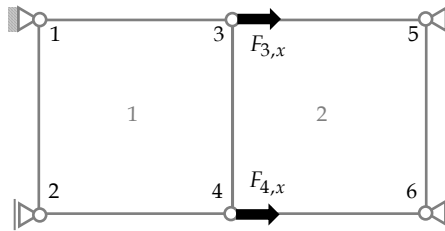


Figure 5. Design domain, boundary conditions and load application of the single rod benchmark

For PTO, the initial relative density of both elements is 0.5, which causes the Young's modulus of the elements to be reduced to 0.125 MPa due to the SIMP material model. In BESO, the initial density of both elements equals 1, which means that the stiffness is not reduced. However, the homogenized stress states in both elements for BESO and PTO are the same:

$$\boldsymbol{\sigma}_{1,\text{hom}} = E_1(x_1)\mathbf{D}_0\mathbf{B}_1\mathbf{u}_1 = \begin{bmatrix} 0.5000 \\ 0.0496 \\ 0 \end{bmatrix}, \quad \boldsymbol{\sigma}_{2,\text{hom}} = E_2(x_2)\mathbf{D}_0\mathbf{B}_2\mathbf{u}_2 = \begin{bmatrix} -0.5000 \\ -0.0496 \\ 0 \end{bmatrix} \quad (28)$$

Since the shear stress equals zero, it is possible to plot the element stresses in the principal stress state, together with the Drucker-Prager yield function that belongs to a tensile and

compressive strength of 1 and 1.25 MPa, respectively, see Figure 6. Note that as such, this figure presents the initial stress states of the elements for a BESO and PTO simulation.

The dotted line in Figure 6 connects the origin with the stress states of the elements, and then continues as a straight line. The value of the Drucker-Prager criterion resembles the distance from the origin to the stress state of the element divided by the distance from the origin to the location where the dotted line in Figure 6 intersects with the Drucker-Prager yield function. For element 1, this Drucker-Prager criterion value equals $\sigma_{eq,1} = 0.4844$, and for element 2, it equals $\sigma_{eq,2} = 0.3744$. This shows that the stress state of element 1 (the element in tension) is closer to material "yielding" than the stress state of element 2 (the element in compression).

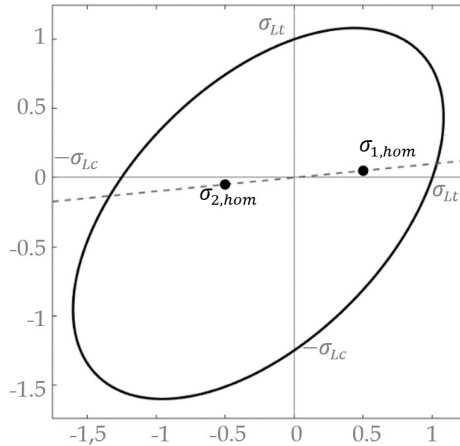





Figure 6. Stress states of elements 1 and 2 in the principle stress space

For PTO, for updating the densities, the material is distributed proportional to the above-mentioned Drucker-Prager equivalent stress value, and thus to element 1, which has the highest value, and is on the tensile side of the structure, see also Table 1.

In the BESO procedure, either element 1 or element 2 must be transformed into a void element, because the Drucker-Prager equivalent stress values after the first analysis are below their limits, see Equation 17. Sensitivities to element 1 are $\partial R_1 / \partial x_1 = -0.2427$ and $\partial R_2 / \partial x_1 = -0.1932$, and sensitivities to element 2 are $\partial R_1 / \partial x_2 = -0.2417$ and $\partial R_2 / \partial x_2 = -0.1813$. As follows from Equation 20, for element 1, a sensitivity of 0.2427 will be selected,

and for element 2, a sensitivity of 0.2417. Now if by Equation 18 a single element must be set to zero, the "delete" threshold value is in between the two sensitivities, and the least sensitive element will be deleted, which is here element 2, which is under compression. Note that element 2 has a lower maximal absolute sensitivity than element 1 because of the following. Firstly, for both elements, the stress constraint for element 1 is the most sensitive to the element density. This is because element 1 is closer to the Drucker-Prager criterion. Secondly, it is common sense that the influence of element 1's density is higher on its stress state than the density of the neighbouring element 2. So element 2 shows the lowest (absolute maximum) effect on the constraint of element 1. In conclusion, for the current situation, with all negative sensitivities, the material is distributed such that the overall increase in constraint values is kept to a minimum (as the sensitivity of element 2 was the lowest, so minimal influence on the constraints). However, if positive sensitivities are present as well (besides negative sensitivities), depending on the ratio of their absolute values, the material might also be distributed such that the increase of the constraint values is maximized.

Table 1. Results of the single rod benchmark for a stress-constrained volume minimization with unequal stress limits

	TTO	BESO	PTO
Stress ratio	$\sigma_{Lc} = 1.25 \sigma_{Lt}$	$\sigma_{Lc} = 1.25 \sigma_{Lt}$	$\sigma_{Lc} = 1.25 \sigma_{Lt}$
Visual output (black = solid, white = void)			
Iterations	51 (2.61 s)	51 (1.60 s)	51 (1.59 s)
Volume fraction	0.46	0.50	0.50

With the above reasoning, table 1 correctly shows that BESO and PTO fail to place material in the optimal position, namely at the compression side. However, TTO is functioning differently (and better). As mentioned earlier, TTO differs from PTO and BESO by using both sensitivities of the objective and constraints, combined with intermediate density values, while making use of the Method of Moving Asymptotes (Svanberg, 1987). In MMA, the gradient information is used to create approximating functions for every iteration k , that together form a convex sub problem with only a single minimum. The approximating constraint functions for the first iteration in the single rod benchmark are plotted in Figure

7, with the "current" densities (0.5) of elements 1 (x_1) and 2 (x_2) on the x - and y -axis, respectively. The actual shape of the stress constraint functions is unknown, therefore, approximation functions are used. Figure 7 also includes (dashed) lines of equal volume, described by $x_2 = V - x_1$, in which V is the total structural volume. The sub problem in Figure 7 is solved by finding x_1 and x_2 values that satisfy the constraints (i.e. that are positioned above both constraint approximation functions), while minimizing the total volume (i.e. as close as possible to the origin). The result is the point $x_1 = 0.6630$, $x_2 = 0.6637$. Using these updated densities, a new set of objective and constraint values is obtained, for which new approximation functions are derived. These new approximation functions lead to new values of x_1 and x_2 , etc. Eventually, solving a sequence of these convex sub problems results in finding a global or local minimum of the optimization problem. For the single rod optimization problem, the suggested solutions by MMA per iteration head further and further towards the left-top of the graph (see also Figure 8 in which some of the iterations are visualized graphically), which means that solving the sequence of sub problems results in a situation in which x_2 becomes (nearly) 1 and x_1 becomes (nearly) 0, i.e. the TTO result of the single rod-simulation is a compressive bar (see Table 1). This compressive bar has a lower volume fraction than the tensile bars that were found using PTO or BESO, so a more optimal solution is obtained. Also, note that TTO considers the sensitivity of the objective with respect to the design variables,

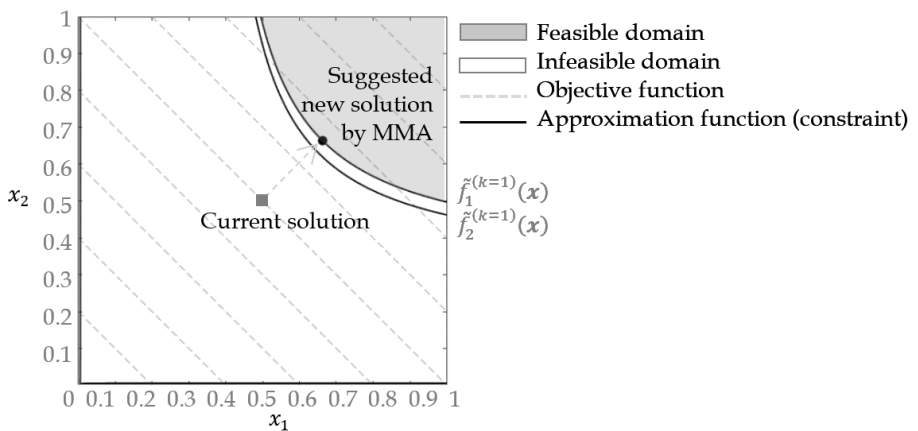


Figure 7. Approximation functions (black lines) of the first iteration of the single rod benchmark, together with the current (grey square) and new (black dot) values of the design variables

meaning that there is an incentive to minimize the structural volume. Differently, in BESO and PTO the volume is not truly minimized, but only adapted based on the value of the stress constraints.

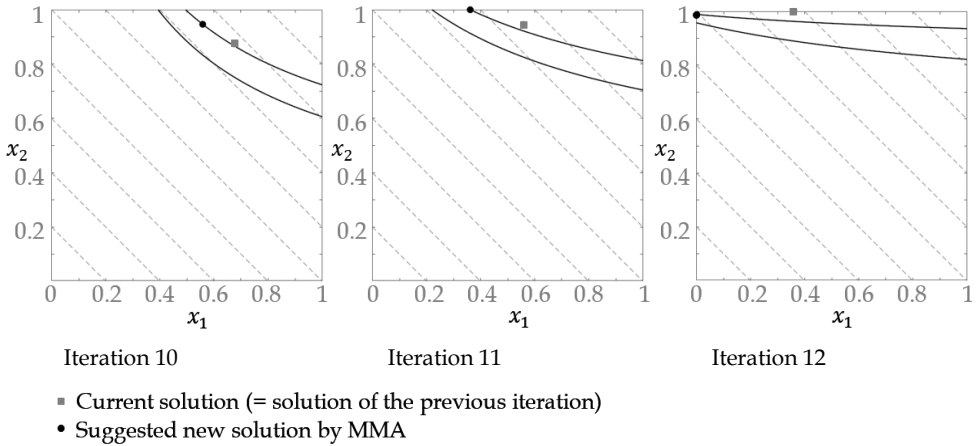


Figure 8. Visualization of the MMA procedure during iterations 10, 11 and 12 of the single rod benchmark. Visualized: approximation functions per iteration (black curves) and results of the previous (grey square) and new (black dot) solutions; these solutions head further and further towards the left top of the graph (i.e. the situation for which $x_1 = 0$ and $x_2 = 1$).

4.4 Four-bar truss benchmark

The second benchmark problem is the so-called ‘four-bar truss’ benchmark, for which the square design domain, four hinged supports, and the single concentrated load at the centre are schematically presented in Figure 9. For the simulations, the 2D design domain is discretized into 20×20 square, bilinear plane stress finite elements of 1×1 mm with $t = 1$ mm, $E = 1$ MPa and $\nu = 0.3$. Furthermore, $L = 20$ mm, $F = 1$ N, $\sigma_{Lt} = 0.75$ MPa, $p = 3$, and $r_{\min} = 1.5$. The four-bar truss benchmark owes its name to its typical cross-like output for symmetric optimization problems. However, for the volume minimization problem with asymmetric stress limits in tension and compression as used here, two of the four members that are usually present in the symmetric solution might be left out. Namely, similar to the previously described single rod benchmark, it is expected that for concrete, the tensile members are left out such that a compression-only structure will be formed, which is likely to have a lower structural volume compared to a tension-only structure. Results are summarized in Table 2. Also for this benchmark, TIO correctly finds the most optimal

solution, whereas PTO and BESO prefer material in the tensile region, for the reasons explained before.

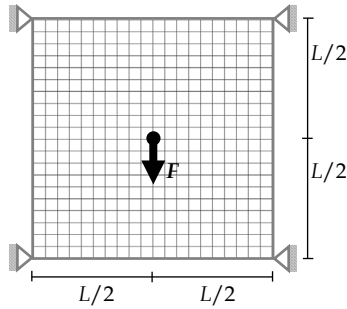
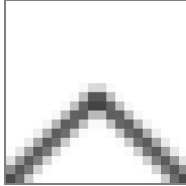
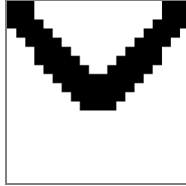
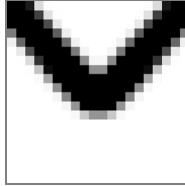


Figure 9. Design domain, boundary conditions and load application of the four-bar truss benchmark

Table 2. Results of the four-bar truss benchmark for a stress-constrained volume minimization with unequal stress limits

	TTO	BESO	PTO
Stress ratio	$\sigma_{Lc} = 3 \sigma_{Lt}$	$\sigma_{Lc} = 3 \sigma_{Lt}$	$\sigma_{Lc} = 3 \sigma_{Lt}$
Visual output			
Iterations	52 (305 s)	169 (13 s)	232 (8 s)
Volume fraction	0.09	0.23	0.28
Stress index*	-0.003	-0.001	-0.000

* Max. Drucker-Prager stress minus limit value; negative value means stress constraints satisfied.

4.5 Two-bar truss benchmark

For the two-bar truss benchmark in Figure 10, necessarily both a tensile and a compressive member are required to distribute the load. The design domain is fixed along the complete bottom by hinges at each finite element node, as schematically presented in Figure 10, for which $L = 80$ mm. Furthermore, a shear load of 1 N is applied in the middle of the upper edge, smoothly distributed over three nodes ($3 \times F = 1$ N). The design domain is meshed

by 20×80 plane stress finite elements of 1×1 mm with $t = 1$ mm, $E = 1$ MPa and $\nu = 0.3$. Furthermore, $\sigma_{Lt} = 0.415$ MPa, $p = 3$, and $r_{\min} = 1.5$.

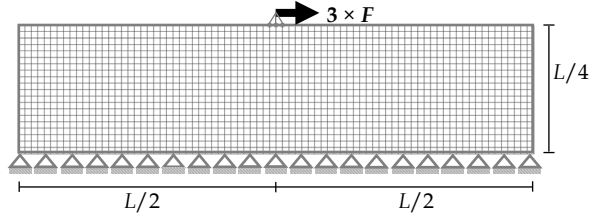


Figure 10. Design domain, boundary conditions and load application of the two-bar truss benchmark

For a material with equal stress limits in tension and compression, the optimum is a symmetric structure with angles of 45° between the bars and the supporting ground-face (Rozvany, 1996). However, for the optimization with asymmetric stress limits, Rozvany (1996) states that the weakest bar (i.e. the tensile bar for concrete) should ideally get a shorter length and a greater width than the stronger (compressive) bar to find the minimum volume. This outcome indeed shows up when using TTO, see Table 3, although the difference in angles between the bars and the supporting ground-face is hardly noticeable for this specific example. However, if a larger difference in compressive and tensile strength is taken and the value of the external load is increased, the angles between the bars and the ground-face will become more distinct, as can be seen in Figure 11. Contrary to TTO, PTO and BESO show longer tensile than compressive bars (as can be seen in Table 3), which is contrarily to the theoretically optimal solution. Besides, these tensile bars do have a greater width than the compressive bars, which corresponds to theory, but which results in a larger final volume of the structure. This is a similar outcome as for the previous benchmarks.

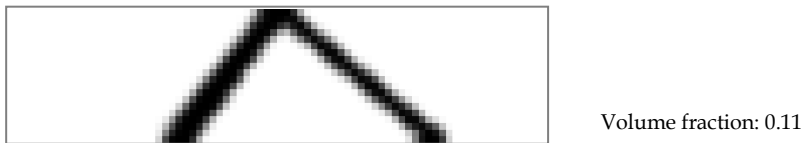



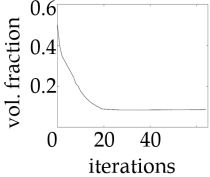
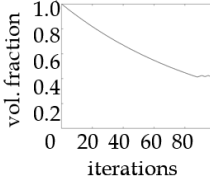
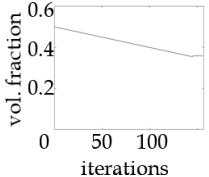


Figure 11. Result of TTO with asymmetric stress limits ($\sigma_{Lc} = 2.58 = 3 \sigma_{Lt}$) and an external force of 1.5 N (all stresses remain below the limits)

Different from TTO, and as shown by Equations 17 and 24, BESO and PTO steer the optimization algorithm based on the maximum stress (peak stress) in the structure. For the two-bar truss problem, the peak stress is near the external load, and so its magnitude might influence the BESO and PTO results. Indeed, if the load in the benchmark above is reduced to 0.9 N, much more optimal structures will be found by PTO (volume fraction = 0.08; a reduction of 81% compared to Table 3) and BESO (volume fraction = 0.10; a reduction of 72%), whereas for TTO the difference is minimal (volume fraction = 0.08; a reduction of 11%).

Table 3. Results of the two-bar truss benchmark for a stress-constrained volume minimization

	TTO	BESO	PTO
Stress ratio	$\sigma_{Lc} = 2 \sigma_{Lt}$	$\sigma_{Lc} = 2 \sigma_{Lt}$	$\sigma_{Lc} = 2 \sigma_{Lt}$
Visual output (See legend Table 2)			
Iterations	65 (1.8 h)	99 (80 s)	157 (8 s)
Volume fraction	0.09	0.42	0.36
Stress index*	-0.001	-0.001	-0.000
Convergence graph			

* Max. Drucker-Prager stress minus limit value; negative value means stress constraints satisfied.

4.6 L-bracket benchmark

The L-bracket benchmark in Figure 12 is an optimization problem for which, at least theoretically, an infinite stress occurs at the sharp inner corner of the design domain, which may be difficult to handle by optimization algorithms. The edges with length $L = 50$ mm are divided into 50 finite elements of 1×1 mm with $t = 1$ mm, $E = 1$ MPa and $\nu = 0.3$. Furthermore, $F = 1$ N, $\sigma_{Lt} = \sigma_{Lc} = 1.5$ MPa, $p = 3$, and $r_{\min} = 1.5$. Table 4 shows the results of the three optimization methods, including a stress plot. For BESO and PTO, the stress singularity at the inner corner remains (for the edge remains sharp) but for TTO, the inner corner is rounded in the optimization process, such that the stress singularity vanishes,

and more elements are utilized up to their full capacity. The reason for PTO to keep the sharp corner is that PTO distributes material to the most highly stressed area(s) in the design domain, which is - for this case - the very high (theoretically infinite) stress at the

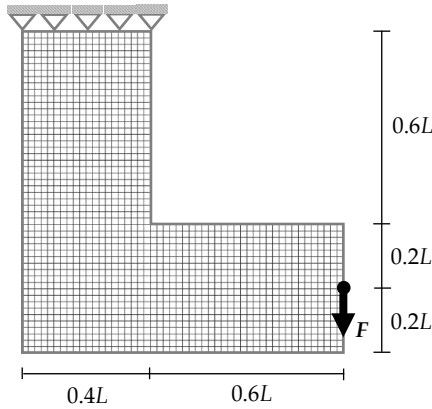


Figure 12. Design domain, boundary conditions and load application of the L-bracket benchmark

Table 4. Results of the L-bracket benchmark for a stress-constrained volume minimization problem

	TTO	BESO	PTO
Stress ratio	$\sigma_{Lc} = \sigma_{Lt}$	$\sigma_{Lc} = \sigma_{Lt}$	$\sigma_{Lc} = \sigma_{Lt}$
Visual output			
Iterations	52 (3.0 h)	110 (242 s)	80 (5 s)
Volume fraction	0.324	0.370	0.393
Stress plot			
Remarks	Homogenized stress: 1.472 MPa, spread out across 3 bars	Max. homogenized stress: peak of 1.491 MPa in inner corner	Max. homogenized stress: peak of 1.500 MPa in inner corner

inner corner. TTO on the other hand uses sensitivity information, which informs that removing material from the inner corner will have a large effect on reducing the peak stresses. Therefore, TTO removes material at the inner corner and rounds it. BESO also uses sensitivity information, but it does not regard the sign of the sensitivity. Instead, it puts material at the locations where the absolute sensitivities are high, which is at the inner corner. It should be noted that BESO studies with stress constraints exist in which the rounded corner does appear. One example is the study of Fan, Xia, Lai, Xia and Shi (2019). However, in that study a p -norm global (symmetrical) stress constraint is used rather than an (asymmetric) stress constraint per element, and the rounded corner only occurs for more stringent stress limits for which a peak stress near the inner corner is still observed.

4.7 MBB beam

Finally, the Messerschmitt-Bölkow-Blohm (MBB) benchmark is used, because it is a classic problem in topology optimization (Sigmund, 2001; Andreassen, Clausen, Schevenels, Lazarov, and Sigmund, 2011). The design domain, boundary conditions, and a single point of load application halfway the symmetric MBB-beam are depicted in Figure 13. For the simulations, the 2D design domain is discretized here into 60×20 square, bilinear plane stress finite elements of 1×1 mm with $t = 1$ mm, $E = 1$ MPa and $\nu = 0.3$. Furthermore, $L = 120$ mm, $F = 1$ N, $\sigma_{Lt} = 1.75$ MPa, $p = 3$, and $r_{\min} = 1.7$. For the optimization problem with asymmetric stress limits in tension and compression, as presented in Table 5, TTO provides a more optimal result with a lower volume fraction compared to BESO and PTO. In the solutions, necessarily both tensile and compressive members must be present, and so no general statement can be made about the required width of the members.

In Table 5, the BESO and PTO results shown are not the final results of the optimization. Instead, from the convergence graph, the optimization results with the minimum volume are selected and presented. Although these solutions are more optimal than the final solutions, the algorithm did not stop the simulations at these points due to a convergence issue. Namely, the convergence criterion for a stable solution is not met at these iterations with the lowest structural volume due to the linear volume in- and decrease that is part of the PTO procedure, and the forced percentual volume in- or decrease for the BESO procedure. Therefore, as mentioned earlier, it is required to study the convergence graph of PTO and BESO after the simulation has finished, to check if the most optimal solution is found. For TTO these issues have not been encountered due to TTO's pure gradient-based character.

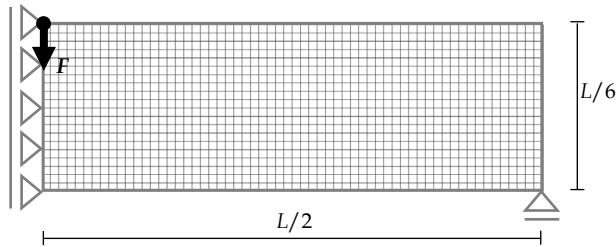


Figure 13. Design domain, boundary conditions, and load application halfway at the MBB beam

Table 5. Results of the MBB beam benchmark for a stress-constrained volume minimization problem

	TTO	BESO	PTO
Stress ratio	$\sigma_{Lc} = 3 \sigma_{Lt}$	$\sigma_{Lc} = 3 \sigma_{Lt}$	$\sigma_{Lc} = 3 \sigma_{Lt}$
Visual output (See legend Table 2)			
Iterations	58 (1.0 h)	135 (65 s)	188 (10 s)
Volume fraction	0.252	0.266	0.375
Stress index*	-0.005	-0.253	-0.091
Convergence graph			

* Max. Drucker-Prager stress minus limit value; negative value means stress constraints satisfied.

4.8 Discussion

In the above benchmarks, all three optimization methods resulted in topologies for which all stress constraints are met, although the solutions differ per method. The single rod and four-bar truss benchmarks ideally result in compression-only structures for a material that has a higher stress limit in compression than in tension. However, Table 1 and Table 2 showed this is only the case for TTO. Differently, PTO naturally distributes the material to the weakest side of the structure if opposite stress states with equal magnitudes are present, since this weakest area is closer to material yielding. BESO, on the other hand, uses the magnitudes of the sensitivities of the constraints with respect to the design variables to steer the simulation, however, their directions (their plus or minus signs) are ignored. Consequently, no distinction is made between positive or negative influences of

the change in relative density on the maximum stress values, so BESO might minimize or maximize this change in the constraint values. Furthermore, neither BESO nor PTO considers the sensitivity of the objective with respect to the design variables, meaning that there is no explicit incentive to minimize the structural volume in these methods. This shortcoming is here partly solved by using a regular mesh and letting the volume decrease if the stresses do not exceed their limits. This solution will, however, not hold if non-regular finite element meshes are used. Contrary to BESO and PTO, TTO explicitly considers the sensitivity of the objective function, and so truly tries to minimize the objective during MMA, resulting in a smooth convergence of the optimization. Furthermore, TTO takes the sensitivities of the stress constraints into account *including* their directions (sign), such that it can steer the minimization of the objective function towards a state in which the increase in constraint values is limited. Consequently, TTO implicitly considers peak stresses, without letting the peak stresses define whether the volume should change. It should be noted, however, that for the current implementations TTO is significantly more time consuming than BESO and PTO: to obtain the solutions in Table 2-5, TTO took on average 62 times as long as BESO and 842 times as long as PTO. For all benchmarks, more than 90% of TTO time was consumed by MMA, in which a dense system of equations of the same size as the number of constraints is solved multiple times in an inner iteration loop. For the currently performed benchmarks, the computational costs of TTO were not considered an issue due to the small scale of the problems. However, for analyses on a more realistic scale, performance improvements should be sought. For example, the computational costs of TTO might be decreased by multithreading, but it is known from literature that topology optimization with local stress constraints and an MMA solver inevitably takes a significant amount of time (Luo & Kang, 2012). Alternatively, solutions like grouped aggregation (Luo & Kang, 2012) or active set strategies (Bruggi & Duysinx, 2012), which either group constraints together or only consider constraints that are near their limits, could be implemented to reduce computational costs. However, one should be careful that the gain in computational time does not come at the cost of an unacceptable loss of local control over the stress distribution, as is for example explained by Le, Norato, Bruns, Ha and Tortorelli (2010).

Another consideration is that also TTO might result in local rather than global optima, because of the MMA procedure. Namely, MMA is a gradient-based method that uses approximation functions to find updated design variables. A typical example of MMA heading towards a local optimum is given in Figure 14, which represents a case with two

design variables and three constraint functions. The suggested solution (away from the current solution) is logical from the perspective of the constraint function gradients and the lowest approximation function, however, clearly steers the solution to the local minimum on the right, instead of the global minimum on the left. As such, it is also possible to find tension-only structures by TTO. However, these less optimal configurations are limited for cases where the approximation functions are inaccurate. On the contrary, BESO and PTO lead to these less optimal configurations all the time, for all cases in which a higher compressive than tensile strength is included.

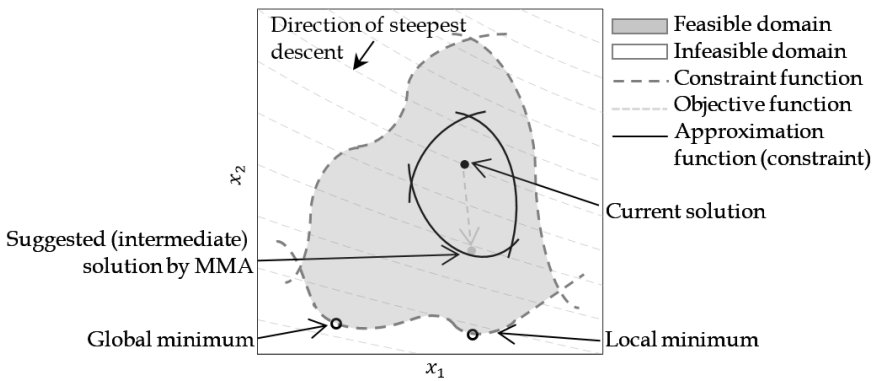


Figure 14. MMA may direct to a local minimum, with the global minimum "out of sight", illustrated for two design variables and three constraints

In conclusion, TTO provides more optimal results for stress-constrained volume minimizations with asymmetric stress limits in tension and compression than BESO and PTO, but shows significant higher computational costs. This is confirmed by the benchmarks used here and in literature. Moreover, TTO is not misled by stress concentrations, whereas BESO and PTO put more material at highly stressed locations, which leads to a higher final volume fraction. Finally, in all benchmarks, the convergence of TTO is smoother than that of BESO and PTO. As a result of the forced material removal that can occur in BESO and PTO, these methods sometimes tend to remove critical elements from the design domain, causing an irreversible increase in the objective value. This forced change of material also makes the volume fractions in the final results of BESO and PTO more sensitive to the presence and magnitude of peak stresses, as compared to TTO.

5 2D application: building façade design

Selecting TTO from the above 2D benchmarks, possibilities can be explored to apply TTO in a design-for-manufacturing tool for real world 3DCP applications. Real world problems, however, have many objectives and constraints. E.g. besides stress constraints, structures should also fulfil deformation and buckling constraints, and possibly other design criteria. Furthermore, a design-for-manufacturing tool especially should include constraints related to the manufacturing process. In this paper a start is made by illustrating the use of TTO in combination with (a) an additional design constraint (daylight) and (b) a print-path generator for the manufacturing process.

5.1 Additional daylight constraint

This section focusses on a case study in which a daylight-score for façade elements (Plak, 2020) is combined with the above presented stress-constrained volume minimization with TTO. So next to the stress constraints, a façade is now also constrained to have a certain minimal daylight score. This daylight score is height dependent since more highly positioned openings cause light to enter further into the room, and so:

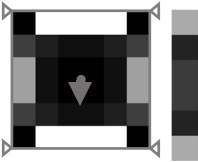
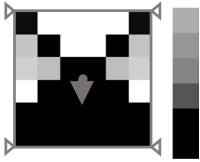
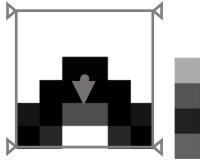
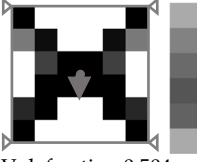
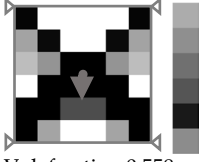
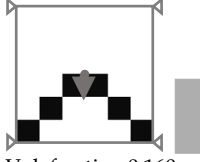
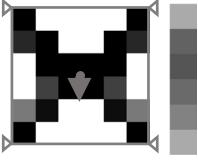
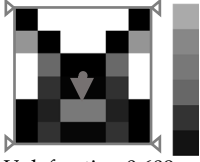
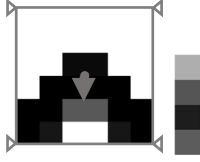
$$s_{dl} = \frac{\sum_{i=1}^N ((1-x_i)p_{dl}h_i)s_{\max}}{\sum_{i=1}^N h_i} \quad (29)$$

in which s_{dl} is the daylight score with $0 \leq s_{dl} \leq s_{\max}$, N is the number of finite elements, p_{dl} is a penalty factor used to steer the optimization as much as possible to black-and-white outcomes (similarly to SIMP), and h_i is the height-factor of element i , which is constant throughout the optimization procedure and is calculated using a linear gradient over the height of the façade, with the lowest values at the bottom and the highest values at the top. This daylight score does not represent a full daylight analysis, but it does provide a useful surrogate model that may serve as a second type of constraint for the design problem. If this daylight factor is to be used in future work, it is recommended to investigate its applicability further, before applying the factor to large-scale real-world optimizations.

First, a parameter study is performed. For this study, a design domain of 6x6 finite elements is used, of 1×1 mm with $t = 1$ mm, $E = 1$ MPa and $\nu = 0.3$. The boundary conditions of the four-bar truss problem (see Figure 9) are applied with $F = 1$ N, $p = 3$,

$p_{dl} = 1$, $s_{\max} = 100$, and filtering is disabled ($r_{\min} = 1$). The lowest stress limit is taken as $\sigma_L = 0.38$ MPa for all simulations in the parameter study. The variable parameters are the prescribed minimum daylight score for the daylight constraint and the (relative) stress limits (i.e. equal strength, higher compressive strength, or higher tensile strength). All results of the parameter study are presented in Table 6. From this parameter study, several trends can be observed.

Table 6. Parameter study for stress- and daylight constrained volume minimization

No daylight constraint	Daylight score > 50%	Daylight score > 75%
$\sigma_{Lc} = \sigma_{Lt}$  Vol. fraction 0.652 Daylight score 34.58 Stress index* -0.000	$\sigma_{Lc} = \sigma_{Lt}$  Vol. fraction 0.646 Daylight score 50.00 Stress index* 0.222	$\sigma_{Lc} = \sigma_{Lt}$  Vol. fraction 0.414 Daylight score 75.00 Stress index* 0.940
$\sigma_{Lc} = 3 \sigma_{Lt}$  Vol. fraction 0.504 Daylight score 50.82 Stress index* -0.000	$\sigma_{Lc} = 3 \sigma_{Lt}$  Vol. fraction 0.558 Daylight score 50.00 Stress index* -0.000	$\sigma_{Lc} = 3 \sigma_{Lt}$  Vol. fraction 0.160 Daylight score 91.78 Stress index* -0.001
$3 \sigma_{Lc} = \sigma_{Lt}$  Vol. fraction 0.504 Daylight score 48.34 Stress index* -0.000 (2)	$3 \sigma_{Lc} = \sigma_{Lt}$  Vol. fraction 0.609 Daylight score 50.00 Stress index* 0.066	$3 \sigma_{Lc} = \sigma_{Lt}$  Vol. fraction 0.419 Daylight score 75.00 Stress index* 0.968 (1)

* Max. Drucker-Prager stress minus limit value; negative value means stress constraints satisfied.

First, it can be concluded that the results are influenced by the presence and magnitude of the minimum daylight score. Namely, the results for which a daylight constraint was added differ from the results without a constraint on the minimum daylight score. Besides, for a simulation with a daylight constraint of 50% (i.e., a constraint that states that the daylight score (s_{dl}) should have a value higher than 50% of s_{max}) the daylight scores are generally lower compared to a simulation with a daylight constraint of 75%. Also, almost inevitably, if more daylight is required, volume fractions become lower.

Secondly, the addition of the daylight constraint generally leads to asymmetrical solutions in which the material tends to be distributed to the bottom of the structure. This tendency seems to be steered by the daylight constraint, because even for a simulation with a higher tensile than compression strength (the bottom row in Table 6), a compression-only structure is shown for a daylight constraint of 75% (marked with (1)). This is different from the situation with only stress-constraints, where more material is distributed to the top of the structure (bottom row, result (2)), which is in line with the conclusions drawn in section 4. More research is required on how MMA manages the conflicting objectives and constraints, and how a more optimal solution can be achieved. See also section 7, future work.

A third aspect that becomes clear in the parameter study is that adding a daylight constraint might result in over-constraining the optimization problem (i.e. not all constraints can be satisfied). Namely, for the simulations without a daylight constraint, the stress constraints are met, as is presented by the negative stress index in Table 6. Note that this stress index is calculated as the maximum Drucker-Prager stress value that is found in the structure minus its limit, so a negative stress index means that all stress constraints in the structure are satisfied. On the other hand, the results of the simulations with both stress- and daylight constraints regularly show violations of the stress constraints (i.e. a positive stress index). In case of violation of the stress constraints, a larger magnitude of the stress index indicates a more severe violation of the stress constraint by the most highly stressed element in the structure. As such, it can also be observed that for a more stringent daylight score, the stress violations generally become higher.

5.2 *Print-path generator*

Besides additional objectives or constraints, a design-for-manufacturing tool should also allow for a translation of an optimized design into a printable geometry. For an illustration of future developments, here the print-path generation tool of Versteeg (2020) is used.

Versteeg's tool translates 2D topology optimization results into printable geometries, including a defined print-path. For this, the geometry is first simplified by removing finite elements with densities lower than 0.5, whereafter a smooth contour line is found through the pixelated solution. Subsequently, members and nodes are identified in the smoothened structure, after which the centrelines and thicknesses of the members are determined.

Using this information, the algorithm then determines the route that the printer should follow to construct the design. By printing at different speeds, the width of each printing layer can be varied from 40 mm to 80 mm. More details can be found in Versteeg (2020).

5.3 *Building façade design: TTO, daylight maximization, print-path*

In this section a case study is presented in which the above-mentioned daylight-score (Plak, 2020) and the print-path generation tool (Versteeg, 2020) are combined with TTO stress-constrained volume minimization. The case study treats a building façade that is subjected to a floor load and a wind load, as presented in Figure 15 (Bouw, 2020). To

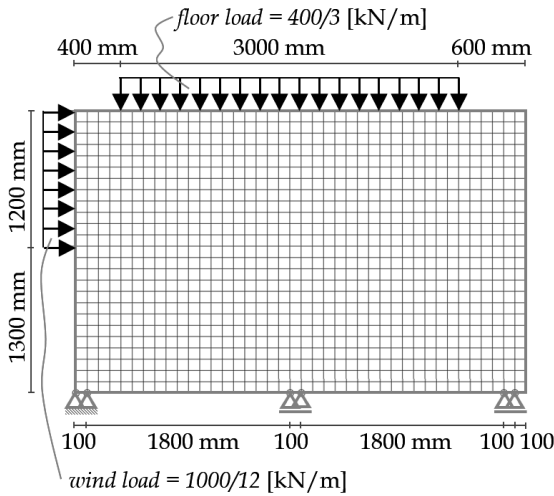


Figure 15. Design domain, boundary conditions, and load application of the façade, including general settings of the simulation

Input variable	Value
Length edge element	100 mm
Element thickness	100 mm
No. of elements hor.	40
No. of elements vert.	25
Young's modulus	1 MPa
Poisson's ratio	0.2
Minimum density	1e-3
Penalty factor SIMP	3.0
Filter radius	1.5
Penalty factor daylight	3.0
s_{\max} (Equation 29)	10
Tensile strength	18.5 MPa
Compressive strength	18.5 MPa

circumvent a possible over-constrained optimization problem, by too competitive constraints, as was seen in the previous section, it was decided to not add the daylight score as a constraint, but to make daylight maximization the objective. Besides, volume minimization is now omitted. Furthermore, it should be mentioned that this case study is regarded as an illustrative application to show the potential of the theory described in the current research, and to steer future research (Section 7). Therefore, no ready-to-use outcomes or thorough analyses of the results are provided yet.

The optimized result for the stress-constrained daylight maximization of the façade in Figure 15 is shown in Figure 16 on the left. And using the print-path generation tool of Versteeg (2020), the print path was obtained as shown in Figure 16 on the right. A façade design results that distributes the required loads; has allowable stresses; a maximized daylight score; and is printable. However, the shape of the printable geometry differs significantly from the pixelated design on the left. In the current study, it was not further investigated how close the printable geometry of Figure 16 is related to the optimal geometry it was based on, because the development and full analysis of the print-path generator is out of the scope of the research here. However, for further developments this should be studied in detail. Namely, removing low-density elements impacts the stress distribution in the structure. Alternatively, it might be beneficial to adapt TTO filtering types that provide better black-and-white solutions, e.g. as shown by Hofmeyer, Schevenels, and Boonstra (2017). On the other hand, developments in the 3DCP industry might lead to the possibility to print several materials simultaneously, or materials with

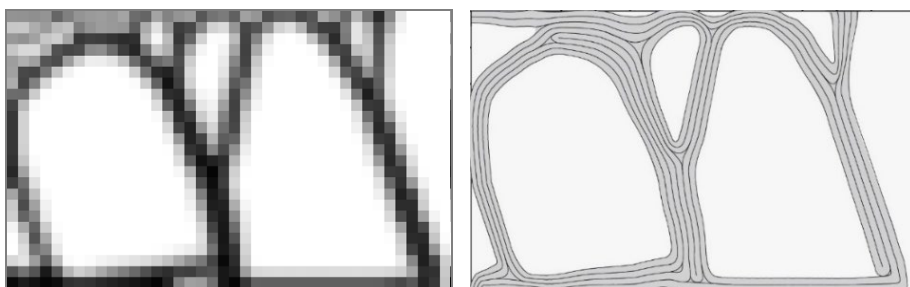


Figure 16. Translation of a topology-optimization outcome (left) into a print-path for 3D concrete printing applications (right), using the print-path generation tool of Versteeg (2020). A facade design results that distributes the required loads; has allowable stresses; a maximized daylight score; and is printable

reduced densities and reduced material properties. If so, grey-scale solutions might also become feasible to print. But all in all, it can be concluded that more research is required before topology optimization and 3DCP can be combined in a design-for-manufacturing tool.

6 Conclusions

The research presented here aims at providing a start in the development of a design-for-manufacturing tool for 3DCP applications, by investigating which topology optimization method provides the most optimal results for a material with asymmetric stress limits in tension and compression. Consequently, three available topology optimization methods have been researched, in which stress constraints are represented by the Drucker-Prager yield criterion. Simulations show that Traditional Topology Optimization (TTO) with the Method of Moving Asymptotes (MMA) by Svanberg (1987) provides more optimal results than BESO and PTO, although this comes at quite higher computational costs. Furthermore, the total volume fraction in BESO and PTO is much more influenced by the presence and magnitude of peak stresses, and BESO and PTO do not show smooth convergence towards the optimal solution. Consequently, to obtain the most optimal results, it is recommended to use TTO for further developments.

To illustrate some possibilities to apply TTO in the field of 3DCP, an additional daylight score constraint/objective was included in a case study, and a print path generation tool was applied. From the case study, it can be concluded that the optimization algorithm can be extended to include more objectives and constraints, however, local optima rather than global optima may be found as a result of the competitive nature of several objectives and constraints. More research is required to find out how to deal with this competitiveness, specifically for cases with asymmetric stress limits in tension and compression.

6.1 Recommendations and future work

Although TTO provides more optimal results than BESO and PTO, it is also by far the most time-consuming method. Therefore, computational costs should be reduced, e.g. via constraint grouping (Luo & Kang, 2012) or active set strategies (Bruggi & Duysinx, 2012) when real-world problems have to be solved. Moreover, the research here did not focus on multi-criteria optimization, and so more research has to be carried out on multi-criteria

optimization with the TTO method, and on how MMA handles trade-offs between competitive constraints.

To develop a truly effective design-for-manufacturing tool for 3DCP, the TTO method itself may be improved as well. For example, a different filter might be applied that provides better black-and-white solutions, such that a practical interpretation of 'grey' material is not required (Hofmeyer, Schevenels, Boonstra, 2017). Furthermore, the structural model of the optimization algorithm might be improved, for example by adding the possibility to include self-weight or multiple load cases. Additionally, for enabling direct printing of the optimized results, manufacturing constraints should be included in the optimization process.

It should be noted that the global optimum of a volume minimization problem with relaxed stress constraints exists of only void elements. However, the strains in these void elements are very large, and so the addition of an additional displacement constraint might be useful.

Finally, based on the research presented here, for façade panels topology optimization for multiple materials (e.g. concrete and insulation) is investigated, including thermal performance as an objective (Youshi, 2021; Youshi 2022). Within that research, also multi-scale modelling of the concrete material is tested (Jia, Misra, Poorsolhjouy, Liu, 2017; Bol 2022).

Acknowledgements

The authors would like to thank Prof. Mattias Schevenels (KU Leuven) for his indispensable effort in explaining critical aspects of topology optimization, and for providing critical feedback during the research. Furthermore, the authors would like to thank Krister Svanberg for providing his implementation of the Method of Moving Asymptotes, which was used in this work.

Literature

- Andreassen, E., Clausen, A., Schevenels, M., Lazarov, B.S., & Sigmund, O. (2011). Efficient topology optimization in Matlab using 88 lines of code. *Structural and Multidisciplinary Optimization*, 43(1), 1-16.
- Bendsøe, M.P., & Kikuchi, N. (1988). Generating optimal topologies in structural design using a homogenization method. *Computer Methods in Applied Mechanics and Engineering*, 71(2), 197-224.
- Bendsøe, M.P., & Sigmund, O. (2003). *Topology optimization: theory, methods, and applications*. Springer, Berlin, Heidelberg.
- Biyikli, E., & To, A.C. (2015). Proportional Topology Optimization: a new non-sensitivity method for solving stress constrained and minimum compliance problems and its implementation in Matlab. *PLoS ONE*, 10(12).
- Bol, R.W.M. (2022). Multi-Scale Material Modelling: Application in Topology Optimization of Structures, M.Sc. thesis Eindhoven University of Technology, Department of the Built Environment, Unit Structural Engineering and Design.
- Bouw, I. (2020). Stress-constrained topology optimization of concrete structures: preliminary study for combining topology optimization and 3D concrete printing. MSc-thesis Eindhoven University of Technology, Department of the Built Environment, Unit Structural Engineering and Design.
- Bruggi, M., & Duysinx, P. (2012). Topology optimization for minimum weight with compliance and stress constraints. *Structural and Multidisciplinary Optimization*, 46(3), 369-384.
- Challis, V.J. (2010). A discrete level-set topology optimization code written in Matlab. *Structural and Multidisciplinary Optimization*, 41(3), 453-464.
- Deaton, J.D., & Grandhi, R.V. (2014). A survey of structural and multidisciplinary continuum topology optimization: post 2000. *Structural and Multidisciplinary Optimization*, 49(1), 1-38.
- Duysinx, P., & Bendsøe, M.P. (1998). Topology optimization of continuum structures with local stress constraints. *International Journal for Numerical Methods in Engineering*, 43(8), 1453-1478.
- Duysinx, P., & Sigmund, O. (1998). New developments in handling stress constraints in optimal material distribution. 7th Symposium on *Multidisciplinary Analysis and Optimization*, AIAA/USAF/NASA/ISSMO, AIAA-98-4906, pp. 1501-1509.

- Fan, Z., Xia, L., Lai, W., Xia, Q., & Shi, T. (2019). Evolutionary topology optimization of continuum structures with stress constraints. *Structural and Multidisciplinary Optimization*, 59, 647-658.
- Hofmeyer, H., Schevenels, M., Boonstra, S. (2017). The generation of hierarchic structures via robust 3D topology optimization. *Advanced Engineering Informatics*, 33, 440-455.
- Jewett, J.L., & Carstensen, J.V. (2019). Topology-optimized design, construction and experimental evaluation of concrete beams. *Automation in Construction*, 102, 59-67.
- Jia, H., Misra, A., Poorsolhjouy, P., & Liu, C. (2017). Optimal structural topology of materials with micro-scale tension-compression asymmetry simulated using granular micromechanics, *Materials & Design*, 115, 422-432.
- Kinomura, K., Murata, S., Yamamoto, Y., Obi, H., & Hata, A. (2020). Application of 3D printed segments designed by topology optimization analysis to a practical scale prestressed pedestrian bridge. In F. P. Bos, S. S. Lucas, R.J.M. Wolfs, & T.A.M. Salet (Eds.), *Second RILEM International Conference on Concrete Digital Fabrication* (pp. 691-700). RILEM Bookseries, 28. Springer, Cham.
- Langelaar, M. (2018). Combined optimization of part topology, support structure layout and build orientation for additive manufacturing. *Structural and Multidisciplinary Optimization*, 57, 1985-2004.
- Le, C., Norato, J., Bruns, T., Ha, C., & Tortorelli, D. (2010). Stress-based topology optimization for continua. *Structural and Multidisciplinary Optimization*, 41, 605-620.
- Liu, Y., Jewett, J.L., & Carstensen, J.V. (2020). Experimental investigation of topology-optimized deep reinforced concrete beams with reduced concrete volume. In F. P. Bos, S. S. Lucas, R.J.M. Wolfs, & T.A.M. Salet (Eds.), *Second RILEM International Conference on Concrete Digital Fabrication* (pp. 691-700). RILEM Bookseries, 28. Springer, Cham.
- Luo, Y., & Kang, Z. (2012). Topology optimization of continuum structures with Drucker-Prager yield stress constraints. *Computers & Structures*, 90-91, 65-75.
- Pastore, T., Menna, C., & Asprone, D. (2020). Combining multiple loads in a topology optimization framework for digitally fabricated concrete structures. In F. P. Bos, S. S. Lucas, R.J.M. Wolfs, & T.A.M. Salet (Eds.), *Second RILEM International Conference on Concrete Digital Fabrication* (pp. 691-700). RILEM Bookseries, 28. Springer, Cham.
- Plak, T.S. (2020). A multi-criteria proportional topology optimization. MSc-thesis Eindhoven University of Technology, Department of the Built Environment, Unit Structural Engineering and Design.
- Rozvany, G.I.N. (1996). Some shortcomings in Michell's truss theory. *Structural Optimization*, 12, 244-250.

- Salet, T.A.M., Ahmed, Z.Y., Bos, F.P., & Laagland, H.L.M. (2018). Design of a 3D printed concrete bridge by testing. *Virtual and Physical Prototyping*, 13(3), 222-236.
- Sigmund, O. (2001). A 99 line topology optimization code written in Matlab. *Structural and Multidisciplinary Optimization*, 21(2), 120-127.
- Sigmund, O. (2007). Morphology-based black and white filters for topology optimization. *Structural and Multidisciplinary Optimization*, 33(4-5), 401-424.
- Svanberg, K. (1987). The method of moving asymptotes – A new method for structural optimization. *International Journal for Numerical Methods in Engineering*, 24(2), 359-373.
- Svanberg, K. (2002). A class of globally convergent optimization methods based on conservative convex separable approximations. *SIAM Journal on optimization*, 12(2). 555-573.
- Versteeg, J. (2020). An integrated approach for topology optimization and print path generation of cable-reinforced 3D printed concrete structures. MSc-thesis Eindhoven University of Technology, Department of the Built Environment, Unit Structural Engineering and Design.
- Xia, L., Xia, Q., Huang, X., & Xie, Y.M. (2018). Bi-directional evolutionary structural optimization on advanced structures and materials: a comprehensive review. *Archives of Computational Methods in Engineering*, 25(2), 437-478.
- Xia, L., Zhang, L., Xia, Q., & Shi, T. (2018). Stress-based topology optimization using bi-directional evolutionary structural optimization method. *Computer Methods in Applied Mechanics and Engineering*, 333, 356-370.
- Xie, Y. M., & Steven, G. P. (1997). *Evolutionary structural optimization*. Springer, London.
- Youshi, M., Hofmeyer, H., & Bruurs, M.J.A.M. (2021). Topology Optimization for Multiple Materials with both Structural and Thermal Objectives to Design 3D Printed Building Panels. Poster *24th Engineering Mechanics Symposium*, October 26, 2021, Arnhem, The Netherlands.
- Youshi, M. (2022). *Topology Optimization for Multiple Materials with Structural and Thermal Objectives to Design 3D Printed Building Elements*. PDEng thesis (SAI 2022/030) Eindhoven University of Technology, Department of the Build Environment, Unit Structural Engineering and Design.

